



# Quantum parity Hall effect in Bernal-stacked trilayer graphene

Petr Stepanov<sup>a,1</sup>, Yafis Barlas<sup>b,1</sup>, Shi Che<sup>a</sup>, Kevin Myhro<sup>c</sup>, Greyson Voigt<sup>c</sup>, Ziqi Pi<sup>c</sup>, Kenji Watanabe<sup>d</sup>, Takashi Taniguchi<sup>d</sup>, Dmitry Smirnov<sup>e</sup>, Fan Zhang<sup>f</sup>, Roger K. Lake<sup>g</sup>, Allan H. MacDonald<sup>h,2</sup>, and Chun Ning Lau<sup>a,2</sup>

<sup>a</sup>Department of Physics and Astronomy, The Ohio State University, Columbus, OH 43210; <sup>b</sup>Department of Physics, Yeshiva University, New York, NY 10033; <sup>c</sup>Department of Physics and Astronomy, University of California, Riverside, CA 92521; <sup>d</sup>National Institute for Materials Science, Ibaraki 305-0044, Japan; <sup>e</sup>National High Magnetic Field Laboratory, Tallahassee, FL 32310; <sup>f</sup>Department of Physics, University of Texas at Dallas, Richardson, TX 75080; <sup>g</sup>Department of Electrical Engineering, University of California, Riverside, CA 92521; and <sup>h</sup>Department of Physics, University of Texas at Austin, Austin, TX 78712-1192

Contributed by Allan MacDonald, March 27, 2019 (sent for review December 12, 2018; reviewed by Andre Geim and Francisco Guinea)

The quantum Hall effect has recently been generalized from transport of conserved charges to include transport of other approximately conserved-state variables, including spin and valley, via spin- or valley-polarized boundary states with different chiralities. Here, we report a class of quantum Hall effect in Bernal- or ABA-stacked trilayer graphene (TLG), the quantum parity Hall (QPH) effect, in which boundary channels are distinguished by even or odd parity under the system's mirror reflection symmetry. At the charge neutrality point, the longitudinal conductance  $\sigma_{xx}$  is first quantized to  $4e^2/h$  at a small perpendicular magnetic field  $B_{\perp}$ , establishing the presence of four edge channels. As  $B_{\perp}$  increases,  $\sigma_{xx}$  first decreases to  $2e^2/h$ , indicating spin-polarized counterpropagating edge states, and then, to approximately zero. These behaviors arise from level crossings between even- and odd-parity bulk Landau levels driven by exchange interactions with the underlying Fermi sea, which favor an ordinary insulator ground state in the strong  $B_{\perp}$  limit and a spin-polarized state at intermediate fields. The transitions between spin-polarized and -unpolarized states can be tuned by varying Zeeman energy. Our findings demonstrate a topological phase that is protected by a gate-controllable symmetry and sensitive to Coulomb interactions.

mirror symmetry is preserved, Landau levels (LLs) belonging to different mirror symmetry representations do not couple.

The complex interplay between the spin, valley, parity, and electronic interactions in ABA graphene suggests the possibility of SPT phases at the carrier neutrality point (CNP) that have not been identified in previous studies (24–29). In this paper, we demonstrate SPT phases in ABA TLG in which mirror symmetry preserves counterpropagating edge modes. We observe a sequence of transitions between different SPT phases that are driven by magnetic field-dependent interactions between electrons close to the Fermi level and the Dirac sea. When mirror symmetry is broken by an out-of-plane displacement field, the two-probe longitudinal conductance decreases dramatically to form a layer-polarized insulator.

Our experiments were performed on dual-gated TLG devices encapsulated between two hexagonal boron nitride (hBN) sheets (Fig. 1B) etched into Hall-bar geometries and with edge contacts (30, 31). The device quality was enhanced by the presence of a local graphite gate underneath the TLG channel, which provides for additional screening of charged impurities and also, enables independent control of the Fermi levels of the channel and the leads (32). The device is very conductive in the absence of

2D materials | quantum Hall effect | topological insulators | symmetry-protected phases | trilayer graphene

In the conventional Hall effect, a charge current combines with a perpendicular magnetic field  $B_{\perp}$  to yield a steady state with a transverse chemical potential gradient. A quantum version of the Hall effect (QHE), in which the chemical potential gradient is replaced by a chemical potential difference between opposite sample edges, can occur when the 2D bulk is insulating. Recently, the Hall effect and the QHE have been generalized from transport of conserved charge to transport of other approximately conserved-state variables, including spin (1, 2) and valley (3, 4); their quantum versions (5–8) are then characterized by spin- or valley-polarized boundary states with different chiralities. For material systems that host these topologically nontrivial phenomena, discrete symmetries play an important role. For example, time-reversal symmetry in the quantum spin Hall effect is essential to protect 1D counterpropagating edge modes from backscattering.

Multiband Dirac systems, such as Bernal- or ABA-stacked trilayer graphene (TLG), afford richer and more exotic symmetry-protected topological (SPT) phases. For instance, in addition to approximate spin and valley symmetries, TLG has an additional discrete mirror symmetry (Fig. 1A) that allows bands to be classified by their parity, the eigenvalue of the operator for reflection in the plane of the middle layer. TLG has two low-energy odd-parity  $\pi$ -bands described by a massless Dirac Hamiltonian with a monolayer graphene (MLG)-like spectrum and four low-energy even-parity bands that exhibit a massive Dirac bilayer graphene (BLG)-like spectrum (9–23) (SI Appendix). As long as

## Significance

The quantum Hall effect, which is characterized by an insulating bulk and chiral edge states, has recently been generalized from transport of charges to transport of other degrees of freedom, leading to quantum spin Hall and quantum valley Hall effects. Here, we report a class of quantum Hall effect, the quantum parity Hall (QPH) effect, in which boundary channels are distinguished by even or odd parity under the system's mirror reflection symmetry. The QPH is realized in charge neutral Bernal- or ABA-stacked trilayer graphene, which displays a striking phase diagram with four different phases, arising from an interplay between topologically protected crystalline symmetry and Coulomb interactions. Our results motivate a search for classes of topological states in van der Waals materials.

Author contributions: P.S., Y.B., S.C., D.S., F.Z., R.K.L., A.H.M., and C.N.L. designed research; P.S., Y.B., S.C., K.M., G.V., Z.P., D.S., F.Z., R.K.L., A.H.M., and C.N.L. performed research; K.W. and T.T. contributed new reagents/analytic tools; P.S., Y.B., F.Z., R.K.L., A.H.M., and C.N.L. analyzed data; and P.S., Y.B., F.Z., R.K.L., A.H.M., and C.N.L. wrote the paper.

Reviewers: A.G., University of Manchester; and F.G., IMDEA Nanociencia.

Conflict of interest statement: K.W. and T.T. are coauthors with A.G. on a 2017 article.

Published under the PNAS license.

<sup>1</sup>P.S. and Y.B. contributed equally to this work.

<sup>2</sup>To whom correspondence may be addressed. Email: macdpc@physics.utexas.edu or lau.232@osu.edu.

This article contains supporting information online at [www.pnas.org/lookup/suppl/doi:10.1073/pnas.1820835116/-DCSupplemental](http://www.pnas.org/lookup/suppl/doi:10.1073/pnas.1820835116/-DCSupplemental).

Published online May 3, 2019.

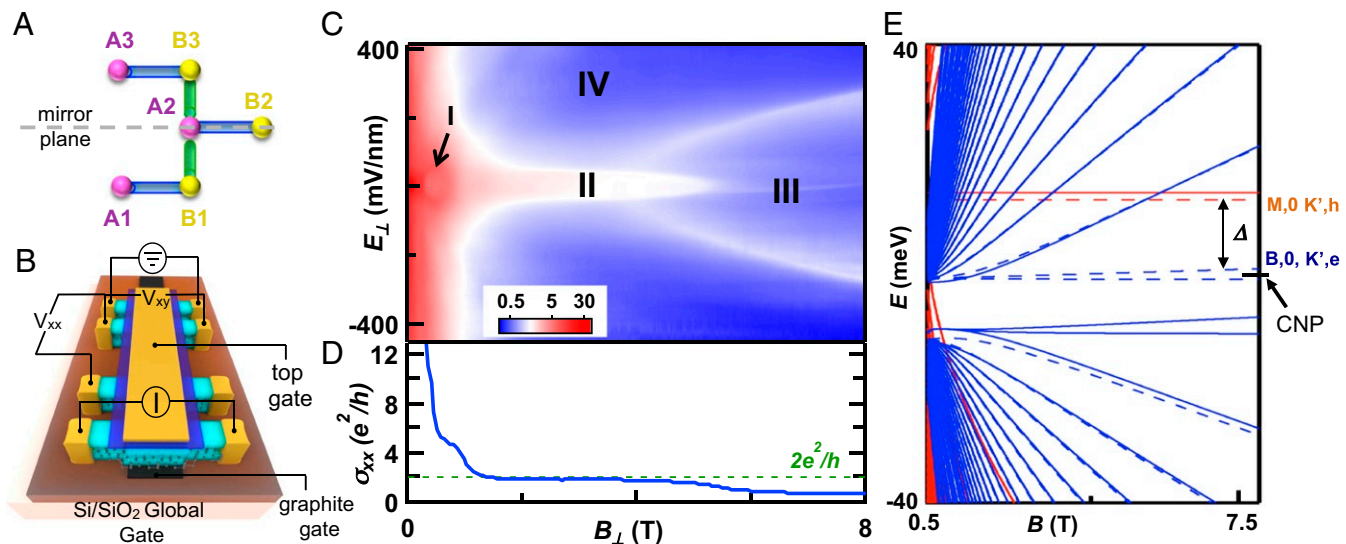


**Fig. 1.** (A) Atomic configurations of ABA TLG. (B) Schematics of an hBN-encapsulated TLG device. (C) Phase diagram  $\sigma_{xx}(E_{\perp}, B_{\perp})$  at the CNP and  $T = 260$  mK. The different electronic phases are labeled I–IV. (D) Line trace  $\sigma_{xx}(B_{\perp})$  at  $E_{\perp} = 0$ . (E) Full parameter  $k \cdot p$  model calculations of the LL energy spectrum as a function of the B field. Dashed (solid) lines indicate  $K$  ( $K'$ ) valley; red and blue lines indicate LL arising from MLG- and BLG-like branches that are odd and even under mirror reflection operation, respectively.

external fields, with longitudinal conductivity  $\sigma_{xx} \sim 1$  mS at the CNP and estimated quantum mobility of  $\sim 80,000 \text{ cm}^2/(\text{V}\cdot\text{s})$  (SI Appendix). By varying top ( $V_{TG}$ ) and bottom gates ( $V_{BG}$ ), we independently control the charge carrier density  $n$  and the external displacement field ( $E_{\perp}$ ). In TLG,  $E_{\perp}$  breaks the mirror symmetry of the ABA film, which allows us to explore the symmetries associated with the topological phases.

To explore topological phases at the CNP, we measure the device's  $\sigma_{xx}$  as a function of  $B_{\perp}$  and  $E_{\perp}$  while maintaining  $N = 0$ . The resulting phase diagram is shown in Fig. 1C. Strikingly, at least four different phases can be identified, which are labeled as I–IV on the plot. The first three phases are observed near zero  $E_{\perp}$ : phase I with quantized conductance  $\sigma_{xx} \sim 4e^2/h$  occurs for very small fields,  $\sim 0.5$  T, and phase II has half the conductance of phase I ( $\sigma_{xx} \sim 2e^2/h$ ) and emerges at intermediate strengths of  $B_{\perp}$  ( $1 < B_{\perp} < 4$  T) (Fig. 1D). As  $B_{\perp}$  increases further, the device transitions to phase III, a resistive state with measured  $\sigma_{xx} \sim 0.5e^2/h$ . In contrast to the first two phases, phase III persists over a wide range in  $|E_{\perp}|$ . All three phases are destroyed by the application of sufficiently large  $|E_{\perp}|$  as the device transitions into an insulating phase IV with  $\sigma_{xx} < 0.1e^2/h$ .

This striking phase diagram identifies different phases by their longitudinal conductivity values and points to SPT phases at the CNP. To understand the nature of these states, we first calculate the band structure of TLG using a continuum  $k \cdot p$  model. The various remote hopping parameters were extracted by fitting calculated spectra to LL crossings in the experimental Landau fan diagram, and they are consistent with previous work (24, 27, 30, 33). The calculated LL spectrum is displayed in Fig. 1E, in which even-parity BLG-like (B) LLs are represented by blue lines, odd-parity MLG-like (M) branches are represented by red lines, and LLs associated with  $K$  and  $K'$  valley LLs are plotted as solid and dashed lines, respectively. A particularly important feature of ABA graphene is the energetic displacement between the even- and odd-parity Dirac points, which arises from remote interlayer hopping and energy differences between stacked and unstacked atoms. In a magnetic field, this displacement places the four-fold degenerate lowest LLs in the MLG-like branch well above the eightfold degenerate lowest LLs in the BLG-like branch. As shown in Fig. 1E, the noninteracting electron ground state for  $B_{\perp} \gtrsim 0.5$  T is a quantum parity Hall (QPH) state with LL filling

factor  $\nu = -2$  for odd-parity states and  $\nu = +2$  for even-parity states. As explained below, the interplay between parity, Zeeman energy, and interactions in these two LLs explains most of the phase diagram.

We first examine phase I, which appears as a small “pocket” for  $0.4 < |B_{\perp}| < 0.8$  T around  $E_{\perp} = 0$  (Fig. 2A); within the pocket,  $\sigma_{xx}$  displays a persistent plateau  $\sim 4e^2/h$  (Fig. 2B and C), while the Hall conductivity  $\sigma_{xy} \sim 0$ , demonstrating ballistic conduction along four edge channels. The  $\sigma_{xx}$  plateau is destroyed by application of  $|E_{\perp}| > 50$  mV/nm, demonstrating

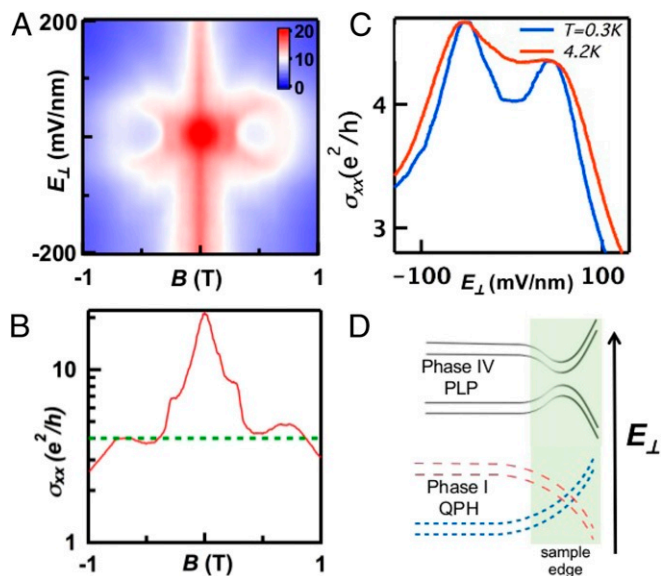


**Fig. 2.** Phase I of TLG. (A) High-resolution  $\sigma_{xx}(E_{\perp}, B_{\perp})$  at low magnetic field  $|B_{\perp}| < 1$ . (B)  $\sigma_{xx}(B_{\perp})$  at  $E_{\perp} = 0$ , showing two plateaus  $\sim 4e^2/h$  at  $B_{\perp} \sim \pm 0.5$  T. (C)  $\sigma_{xx}(E_{\perp})$  at  $B_{\perp} = -0.57$  T. Blue and red lines are taken at 260 mK and 4.2 K, respectively. (D) Schematic of counterpropagating edge states consisting of  $0 -$  LL in the MLG-like band and  $0 +$  in the BLG-like band. The lower and upper schematics illustrate the edge states at zero  $E_{\perp}$  and large  $E_{\perp}$ , respectively. PLP, partially layer polarized.

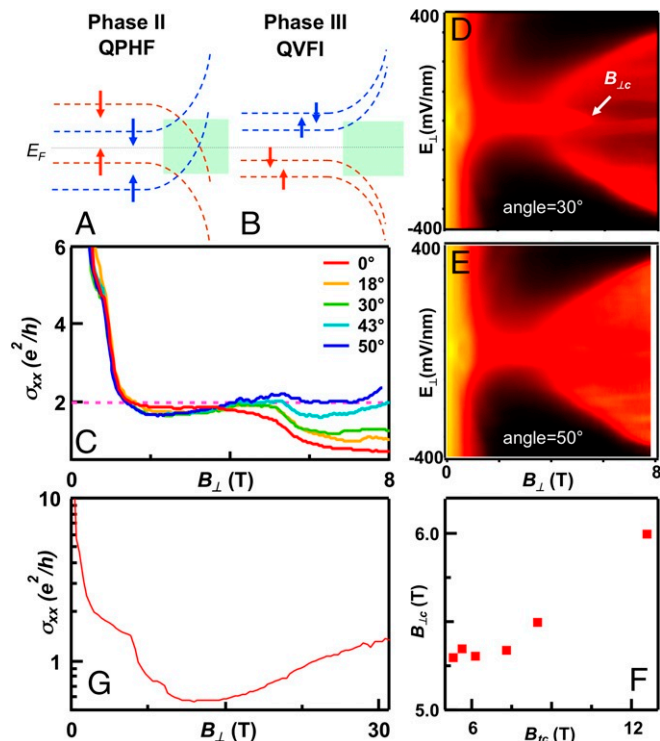


**Fig. 3.** Phases II and III of TLG. (A and B) Schematics of edge-state configurations for phases II and III, respectively. (C)  $\sigma_{xx}(E_{\perp}, B_{\perp})$  at different tilt angles. (D and E)  $\sigma_{xx}(E_{\perp}, B_{\perp})$  at tilt angles  $\theta = 30^{\circ}$  and  $50^{\circ}$ , respectively. Color scale: black, low conductance; red, high conductance. (F) Critical field  $B_{\perp,c}$  for transition between phases II and III vs. total magnetic field  $B_t$ . (G) High field dependence  $\sigma_{xx}(B_{\perp})$  at  $\theta = 0$  for  $B_{\perp}$  up to 31 T.

that it is protected by mirror symmetry. These two properties identify phase I as the spin-unpolarized noninteracting QPH effect ground state expected on the basis of single-particle physics. The quantized  $\sigma_{xx}$  is associated with two even-parity and two odd-parity chiral edge states that propagate from source to drain along opposite edges (Fig. 2D). These approximately spin-degenerate counterpropagating edge states are protected against backscattering by an underlying crystalline symmetry, since they correspond to different representations of the mirror reflection symmetry of the TLG crystal lattice that is preserved at  $E_{\perp} = 0$ . (The slight deviation of  $\sigma_{xx}$  from the quantized value may be accounted for by the presence of disorder that breaks mirror symmetry.) In the presence of a finite displacement field, backscattering between counterpropagating states is allowed, the conductance is quickly reduced to a small value, and the ground state is a partially layer-polarized ordinary insulator.

As  $B_{\perp}$  increases from 1 to 5 T,  $\sigma_{xx}$  drops to  $\sim 2e^2/h$ , signaling a reduction in the number of chiral channels from four in phase I to two in phase II (Fig. 1D). This reduction in  $\sigma_{xx}$  is not expected in a noninteracting electron theory and can be explained only by taking Coulomb interactions into consideration. Two aspects play an essential role: (i) intra-LL interactions along with Zeeman energy can stabilize strongly spin-polarized monolayer-like and bilayer-like  $N = 0$  LLs, and (ii) exchange interactions between the  $N = 0$  LLs and Dirac sea induce a magnetic field-dependent change in the energy separation between LLs with different parity and in the BLG-like case, different orbital character. The latter effect, which also plays a role in phase I by selecting  $N = 0$  BLG-like LLs for occupation over  $N = 1$  LLs, can be captured by adding self-energy corrections (33–35) to the electron and hole LL energies that are larger for  $N = 1$  in the BLG-like case.

These shifts, which are related to the established Dirac velocity enhancement in graphene monolayers in the absence of a field, have the same sign as the carrier and therefore, lower the MLG-like LL energies while raising the BLG-like LL energies (detailed calculations are in *SI Appendix*). For intermediate  $B_{\perp}$ , the (M, h,  $\uparrow$ ) LL is occupied in preference to the orbital  $N = 0$  (B, e,  $\downarrow$ ) LL (Fig. 3A). Phase II has  $\nu = -1$  for odd parity because of an empty spin  $\downarrow$  LL and  $\nu = +1$  for even parity because of an occupied spin  $\uparrow$  LL; therefore, it has counterpropagating edge states with opposite spin and opposite parity, explaining its accurate conductance quantization. We classify phase II as a quantum parity Hall ferromagnet (QPHF).

The quantized conductance of both phases I and II is suppressed by application of a large  $|E_{\perp}|$ . Because  $|E_{\perp}|$  breaks mirror symmetry, edge conduction is no longer protected by crystal symmetry when  $|E_{\perp}| \neq 0$ . Because the  $|E_{\perp}| \neq 0$  suppression occurs to phase II, we conclude that spin-rotational invariance, which would otherwise protect ballistic conduction at finite  $|E_{\perp}|$ , must be broken by spin-orbit coupling in our samples. Even with spin-orbit coupling, mirror symmetry protects the  $|E_{\perp}| = 0$  spin-polarized counterpropagating states. For particles with spin,  $\hat{M}^2 = -1$ , where  $\hat{M}$  is the mirror symmetry operator (*SI Appendix*), with eigenvalues  $\pm i$  for the even-parity and  $\mp i$  for the odd-parity up-spin (down-spin) eigenstates. Therefore, in the QPHF phase, the projected mirror symmetry operator  $\bar{M}$  satisfies  $\bar{M}^2 = -1$ , providing an effective Kramer degeneracy for the QPHF phase. When  $|E_{\perp}| \neq 0$ , the spin-polarized edge states intermix due to spin-orbit coupling, which was originally forbidden due to the mirror symmetry. Since classification on the basis of mirror symmetry is not relevant at  $|E_{\perp}| \neq 0$ , we identify phase

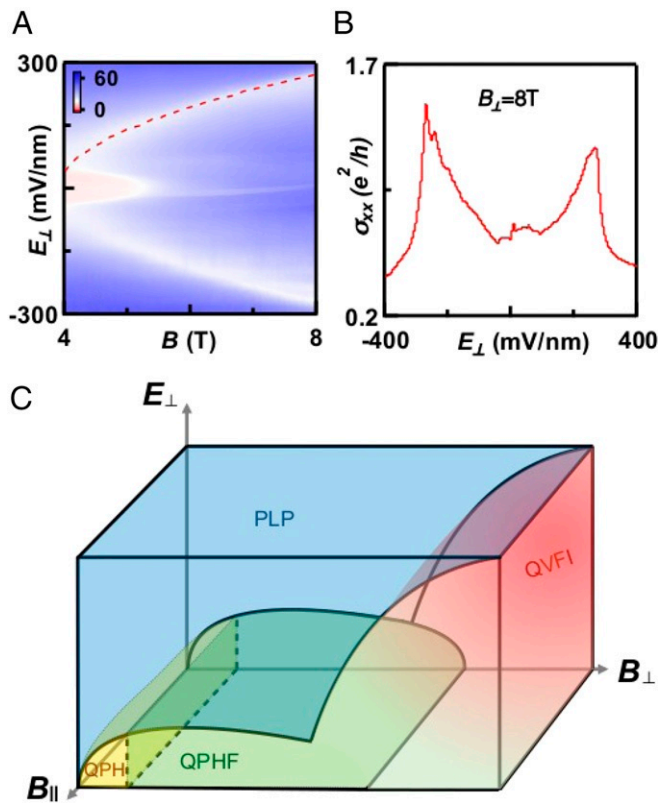


**Fig. 4.** Phase IV and overall phase diagram. (A)  $\sigma_{xx}(E_{\perp}, B_{\perp})$  at the tilt angle  $\theta = 0^{\circ}$  for  $4 \leq B_{\perp} \leq 8$  T. The dotted line is plotted using  $E_{\perp}(\text{mV/nm}) = 135\sqrt{B_{\perp} - 4}$ . (B) Line trace  $\sigma_{xx}(E_{\perp})$  at  $B_{\perp} = 8$  T. (C) Schematics of the phase diagram of charge neutral TLG as a function of  $E_{\perp}$ ,  $B_{\perp}$ , and  $B_{\parallel}$ . PLP, partially layer polarized.

IV as a partially layer polarized ordinary insulator state with no chiral edge channels and no QPH effect as shown in the upper schematic in Fig. 2D.

For even larger  $B_{\perp}$ , electronic interactions become stronger, further depressing the (M, h) while elevating the (B, e) LL energies. When both spin polarizations of the former are occupied and both spin polarizations of the latter are empty, there are no longer counterpropagating edge states, as all of the even-parity electron LLs are above the odd-parity hole LLs (Fig. 3B). This leads to an insulating phase, phase III, with valley polarization within each Dirac band but no parity polarization. Phase III is a spin-unpolarized quantum valley ferromagnetic insulator (QVFI), which has  $\sigma_{xx} \sim 0.5e^2/h$ ; we attribute the finite  $\sigma_{xx}$  to weak intervalley scattering and disorder.

Stability conditions for the  $|E_{\perp}|=0$  phases that we observe can be expressed (SI Appendix) in terms of dressed LL energies:

$$\begin{aligned} \Sigma &\leq \Delta - E_Z && \text{Phase I (QPH)} && [1] \\ \Delta - E_Z &\leq \Sigma \leq \Delta + E_Z && \text{Phase II (QPHF)} && [2] \\ \Sigma &\geq \Delta + E_Z && \text{Phase III (QVFI)} && [3] \end{aligned}$$

where  $E_Z$  is the Zeeman energy,  $\Sigma$  is the relevant self-energy sum related to interactions with the Dirac sea, and  $\Delta$  is the separation between the spin-degenerate lowest LLs between the even- and odd-parity branches in the zero-field limit. From fitting LL crossing points (26, 29),  $\Delta$  is estimated to be 14.5 meV. Transitions between the phases occur at equality. Despite their apparent simplicity, these equations capture all of the salient features of our experimental observations.

Eq. 3 implies that the transition between phases II and III is tunable by the Zeeman energy. Adding an in-plane magnetic field  $B_{\parallel}$  increases the right-hand side of Eq. 3 while leaving  $\Sigma$ , which increases with  $B_{\parallel}$ , unchanged. It follows that phase III should be driven to phase II by a sufficiently large  $B_{\parallel}$ . To test this prediction, we have measured  $\sigma_{xx}(E_{\perp}, B_{\perp})$  at different magnetic field tilt angles  $\theta$ . The line traces  $\sigma_{xx}(B_{\perp})$  are shown in Fig. 3C, and two representative datasets at  $\theta = 30^{\circ}$  and  $50^{\circ}$  are shown in Fig. 3D and E. As expected, as  $B_{\parallel}$  increases, the device crosses over to a conductive state that has  $\sigma_{xx} \sim 2e^2/h$ . Moreover, the critical  $B_{\perp,c}$  value at which the transition to the QVFI state occurs increases with increasing  $B_{\parallel}$ , in agreement with Eq. 3 (Fig. 3F). We emphasize that, although superficially resembling the in-plane field phase transitions observed in MLG (36) and BLG (37), this transition has a fundamentally different nature—instead of crossing over from a canted antiferromagnetic insulator to a ferromagnet in thinner graphene systems, TLG transitions from a spin-unpolarized QVFI to a QPHF. Another important prediction of Eq. 3 is that, since  $\Sigma$  varies approximately like  $\sqrt{B_{\perp}}$  (SI Appendix), while  $E_Z$  scales linearly with  $B_{\perp}$ , phase II should reemerge at fields stronger than we have discussed so far. This is exactly what we observe as

nonmonotonic dependence of  $\sigma_{xx}$  at very large  $B_{\perp}$ . As plotted in Fig. 3G,  $\sigma_{xx}$  reaches a minimum at 12.5 T and then, increase almost linearly as  $B_{\perp}$  increases to 31 T as the device reenters phase II.

Finally, we find that, at large  $B_{\perp}$ , the behavior of the conductivity as a function of displacement field is not monotonic. As  $E_{\perp}$  increases,  $\sigma_{xx}$  first rises to  $\sim 1.5e^2/h$  and then, drops sharply to  $\sim 0.1e^2/h$  (Fig. 4B). The position in  $(E_{\perp}, B)$  space of the local conductivity peak that separates these two regimes can be described phenomenologically by the equation  $E_{\perp}$  (millivolts per nanometer) =  $135\sqrt{B_{\perp}(\text{Tesla})} - 4$  (dotted line in Fig. 4A). The nonmonotonic  $\sigma_{xx}(E_{\perp})$  dependence demonstrates that the first-order phase transition between the spin-unpolarized strong field state and the spin-polarized intermediate field is tuned in favor of the spin-polarized state by nonzero values of  $E_{\perp}$ . A conductivity peak at the transition is expected due to boundary-state transport along domain walls that separate states with zero and nonzero values of the valley Hall conductivity.

The multiple phases observed in the rich phase diagram arise from an intricate interplay between spin and crystalline symmetries, localization, Zeeman energy, exchange interactions, and self-energies of bands with different parities. Multiband Dirac systems, such as ABA-stacked multilayer, provide a rich playground to realize exotic symmetry-protected interacting topological phases (38). Additionally, our observations open the possibility of discovering a plethora of gate-tunable SPT phases protected by point and space group symmetries in 2D crystals and heterostructures.

## Materials and Methods

ABA-stacked TLG and few-layer hBN are mechanically exfoliated from bulk crystals onto Si/SiO<sub>2</sub> substrates. We use a dry-transfer technique to assemble hBN/TLG/hBN stacks. Electron beam lithography and reactive ion etching by sulfur hexafluoride gas plasma are used to define the multiterminal Hall-bar geometry. TLG is then coupled to Cr/Au metallic contacts and Cr/Au top gates. The devices are measured in He3 refrigerators using standard lock-in techniques.

**ACKNOWLEDGMENTS.** We thank Maxim Kharitonov for discussions. The experiments are supported by Department of Energy (DOE) Basic Energy Sciences (BES) Division Grant ER 46940-DE-SC0010597. The theoretical works and collaboration between theory and experiment are enabled by Spin and Heat in Nanoscale Electronic Systems, which is an Energy Frontier Research Center funded by DOE BES Award SC0012670. Part of this work was performed at the National High Magnetic Field Lab, which is supported by NSF/Division of Materials Research-0654118, the State of Florida, and the DOE. Growth of hexagonal boron nitride crystals was supported by the Elemental Strategy Initiative conducted by the Ministry of Education, Culture, Sports, Science and Technology and a Grant-in-Aid for Scientific Research on Innovative Areas "Science of Atomic Layers" from Japan Society for the Promotion of Science. Work in Austin was supported in part by DOE Division of Materials Sciences and Engineering Grant DE-FG03-02ER45958 and Welch Foundation Grant F1473. F.Z. was supported by Army Research Office Grant W911NF-18-1-0416 and University of Texas at Dallas research enhancement funds.

- Dyakonov MI, Perel VI (1971) Possibility of orienting electron spins with current. *Phys JETP Lett* 13:467–469.
- Dyakonov MI, Perel VI (1971) Current-induced spin orientation of electrons in semiconductors. *Phys Lett A* 35:459–460.
- Mak KF, McGill KL, Park J, McEuen PL (2014) The valley Hall effect in MoS<sub>2</sub> transistors. *Science* 344:1489–1492.
- Gorbachev RV, et al. (2014) Detecting topological currents in graphene superlattices. *Science* 346:448–451.
- Konig M, et al. (2008) The quantum spin Hall effect: Theory and experiment. *J Phys Soc Jpn* 77:031007.
- Qiao ZH, Tse WK, Jiang H, Yao YG, Niu Q (2011) Two-dimensional topological insulator state and topological phase transition in bilayer graphene. *Phys Rev Lett* 107:256801.
- Ding J, Qiao ZH, Feng WX, Yao YG, Niu Q (2011) Engineering quantum anomalous/valley Hall states in graphene via metal-atom adsorption: An ab-initio study. *Phys Rev B* 84:195444.
- Zhang F, Jung J, Fiete GA, Niu QA, MacDonald AH (2011) Spontaneous quantum Hall states in chirally stacked few-layer graphene systems. *Phys Rev Lett* 106:156801.
- Apalkov VM, Chakraborty T (2012) Electrically tunable charge and spin transitions in Landau levels of interacting Dirac fermions in trilayer graphene. *Phys Rev B* 86:035401.
- Bao W, et al. (2011) Stacking-dependent band gap and quantum transport in trilayer graphene. *Nat Phys* 7:948–952.
- Cong C, et al. (2011) Raman characterization of ABA- and ABC-stacked trilayer graphene. *ACS Nano* 5:8760–8768.
- Henriksen EA, Nandi D, Eisenstein JP (2012) Quantum Hall effect and semimetallic behavior of dual-gated ABA-stacked trilayer graphene. *Phys Rev X* 2:011004.
- Jhang SH, et al. (2011) Stacking-order dependent transport properties of trilayer graphene. *Phys Rev B* 84:161408.
- Koshino M, McCann E (2009) Gate-induced interlayer asymmetry in ABA-stacked trilayer graphene. *Phys Rev B* 79:125443.
- Lee Y, et al. (2014) Competition between spontaneous symmetry breaking and single-particle gaps in trilayer graphene. *Nat Commun* 5:5656.
- Liu Y, Goolaup S, Murapaka C, Lew WS, Wong SK (2010) Effect of magnetic field on the electronic transport in trilayer graphene. *ACS Nano* 4:7087–7092.

